JMEPEG (2020) 29:6085–6100
https://doi.org/10.1007/s11665-020-05067-3

©ASM International
1059-9495/$19.00

Surface Chemistry and Semiconducting Properties of Passive Film and Corrosion Resistance of Annealed Surgical Stainless Steel

Rodrigo Kenji de Oliveira, Olandir Vercino Correa, Mara Cristina Lopes de Oliveira, and Renato Altobelli Antunes

(Submitted March 25, 2020; in revised form June 24, 2020; published online September 1, 2020)

ASTM F-139 surgical stainless steel was subjected to annealing treatments at 700 °C for different times. The effect of annealing on the chemical composition of the passive film was evaluated by x-ray photoelectron spectroscopy. The correlation of the surface chemistry with the corrosion behavior and semiconducting properties of the passive film was also investigated. Potentiodynamic polarization tests were conducted in phosphate-buffered solution at 37°C. The semiconducting character of the passive film was assessed by the Mott–Schottky approach. The microstructure of the annealed samples was characterized by optical microscopy. The grain size increased after annealing, but the differences between each annealing condition were not significant and could not be associated with the corrosion behavior of the annealed samples. The corrosion resistance was improved depending on the heat treatment condition due to compositional changes of the passive film upon annealing. The best corrosion properties were observed after annealing for 8 h which was ascribed to Cr_2O_3, MoO_3 and FeO enrichment in the passive film.

Keywords annealing treatments, corrosion, Mott–Schottky, surface chemistry

1. Introduction

Austenitic stainless steels are commonly employed as biomedical devices especially for temporary applications such as plates and screws during fracture healing (Ref 1, 2). The surgical grade ASTM F-139 is the standard material for this usage owing to its adequate set of attributes relying on its mechanical strength, reasonable corrosion resistance, ease of manufacturing and low cost (Ref 3-5). It is, though, well known that it is prone to pitting corrosion in chloride-containing electrolytes such as the body fluid (Ref 6, 7). Stress corrosion cracking and corrosion fatigue of surgical stainless steels are often associated with the nucleation and growth of pits (Ref 8-10). It is, therefore, important to decrease its pitting corrosion susceptibility in order to reduce the risk of premature failures.

Annealing treatments can affect the corrosion resistance of stainless steels. Microstructural changes originated from the heat treatments are closely related to the corrosion properties. Deng et al. (Ref 11) investigated the effect of annealing treatments on the pitting corrosion resistance of a super duplex stainless steel. Complex microstructural transformations can be triggered by annealing, such as the formation of sigma phase and chromium nitrides. Pit nucleation sites were, therefore, dependent on the annealing temperature related to the formation of such new phases. Tan et al. (Ref 12) have also found that annealing of super duplex stainless steel has markedly affected its pitting corrosion behavior due to microstructural transformations and also the contents of passivating elements such as chromium and molybdenum dissolved in the crystalline phases. Grain growth is another important feature arising from annealing. Aghuy et al. (Ref 13) reported that grain refinement of the austenitic 304L grade decreased metastable pit frequency by improving the stability of the passive film. By contrast, the probability of stable pit growth increased and pitting potential was little affected by grain refinement. Bitondo et al. (Ref 14), in turn, have found that annealing treatments of ferritic stainless steel grade 444 did not affect the grain size and distribution of inclusions. As a consequence, the corrosion resistance was not influenced by annealing.

The aforementioned effects of annealing on the corrosion properties of stainless steels allow one to hypothesize that it could be advantageously explored as a mean to improve the stability of the passive film by properly controlling its composition and/or the grain size of the treated material. These effects are not deeply known for surgical stainless steels. A great concern would arise from grain growth as the fatigue resistance is enhanced for refined microstructures. One further question arises from this scenario regarding the possible influence of annealing on the diffusivity of point defects through the passive film, its semiconductive character and doping density. Such aspects are also reported to deeply affect the corrosion behavior of stainless steels (Ref 15, 16) and can be assessed by the well-known Mott–Schottky approach (Ref 17, 18).

The aim of the present work was to investigate the effect of annealing treatments on the surface chemistry, semiconducting properties of the passive film and the corrosion behavior of the ASTM F-139 surgical stainless steel. This steel was chosen

Rodrigo Kenji de Oliveira, Mara Cristina Lopes de Oliveira, and **Renato Altobelli Antunes**, Centro de Engenharia, Modelagem e Ciências Sociais Aplicadas (CECS), Universidade Federal do ABC (UFABC), Santo André, SP 09210-580, Brazil; and **Olandir Vercino Correa**, Centro de Ciência e Tecnologia de Materiais (CCTM) – Instituto de Pesquisas Energéticas e Nucleares (IPEN/CNEN-SP), São Paulo, SP, Brazil. Contact e-mail: renato.antunes@ufabc.edu.br.

Table 1 Samples description

Sample	Description	Temperature, °C	Time, h
AR	As-received	…	…
SA	Solution-annealed	1050	1
A-1h	Solution annealing at 1050°C followed by annealing	700	1
A-8h	Solution annealing at 1050°C followed by annealing	700	8
A-24h	Solution annealing at 1050°C followed by annealing	700	24

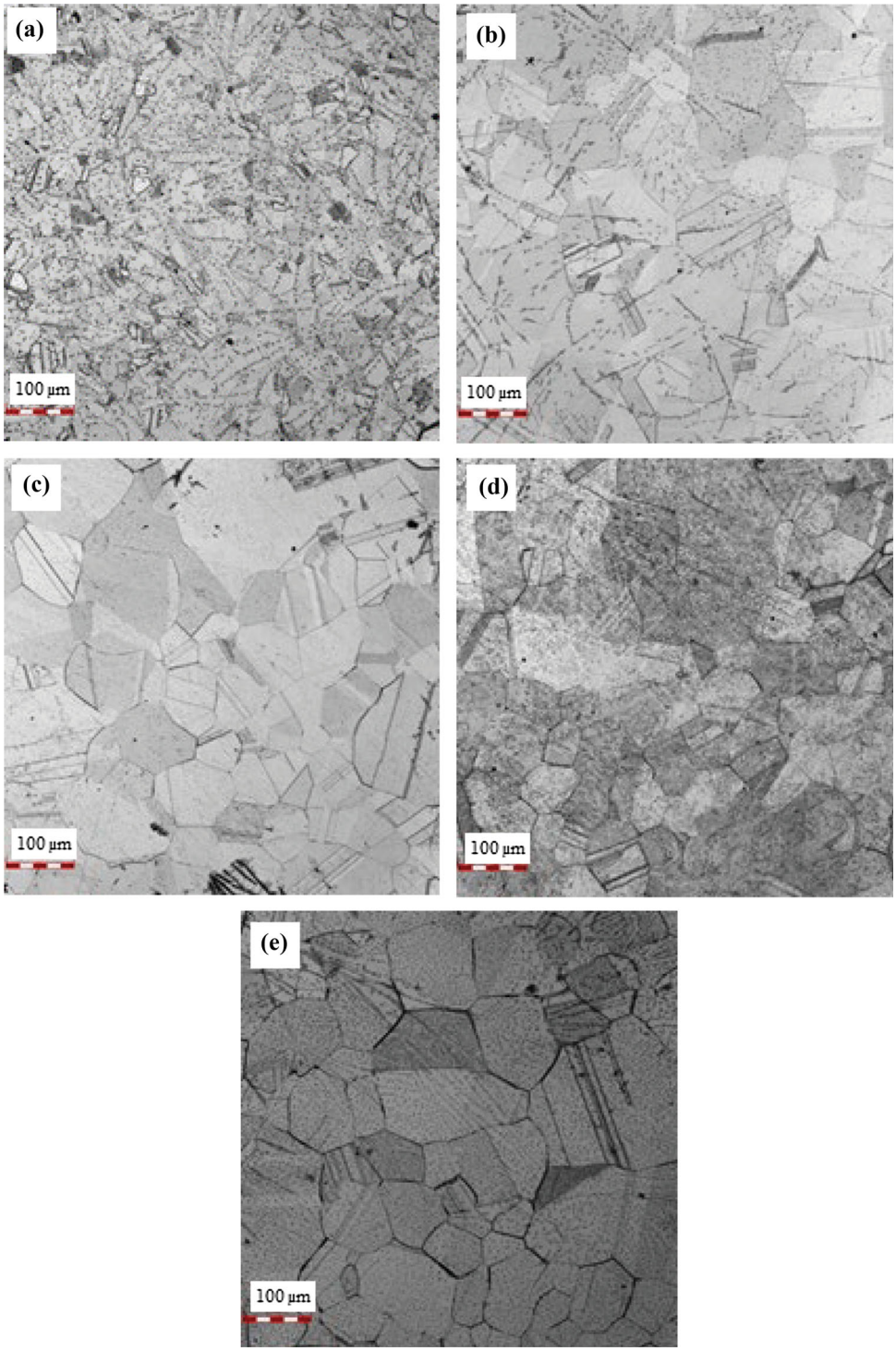

Fig. 1 Optical micrographs showing the microstructures of the: (a) AR; (b) SA; (c) A-1h; (d) A-8h; (e) A-24h

based on its widespread use as surgical implants in the form of sheet and strips. X-ray photoelectron spectroscopy (XPS) was employed to assess the surface chemical composition of as-received and annealed samples. The corrosion properties were evaluated by potentiodynamic polarization. The Mott–Schottky approach was employed to assess the semiconductive properties of the passive film.

2. Materials and Methods

2.1 Material and Heat Treatments

The ASTM F-139 stainless steel plate (thickness of 2 mm) used in the present work was purchased from Acnis (Brazil). Small rectangular pieces with approximate dimensions of 0.70 cm × 1.0 cm were cut from the original plate using a silicon carbide blade in a conventional cutoff machine.

Solution annealing was carried out in a tubular furnace under argon atmosphere at 1050 °C for 1 h, followed by water quenching. The solution-annealed specimens were, next, subject to annealing at 700 °C for 1 h, 8 h and 24 h, followed by natural cooling outside the furnace. Sample designation is shown in Table 1.

Table 2 Grain sizes of the AR and heat-treated samples

Sample	Grain size, μm
AR	24 ± 5
SA	51 ± 10
A-1h	53 ± 4
A-8h	63 ± 4
A-24h	65 ± 8

2.2 Electrochemical Tests

Firstly, a copper wire was connected to one face of the specimens using a colloidal silver paste to promote electrical contact. Next, this set was embedded in cold-curing epoxy resin. After complete curing, the specimens were wet ground using silicon carbide (SiC) papers up to grit 2400. All tests were carried out in an Autolab M101 potentiostat/galvanostat using a conventional three-electrode cell setup with the ASTM F-139 specimens as the working electrodes, a platinum wire as the counter electrode and Ag/AgCl as reference. The tests were conducted in a phosphate-buffered solution (NaCl 82 g L^{-1}, Na_2HPO_4 10.5 g L^{-1}, $NaH_2PO_4{\cdot}H_2O$ 3.55 g L^{-1}) at 37 °C. Samples remained immersed for 24 h before the tests to ensure a steady state condition.

One set of experiments consisted an initial monitoring period of the open-circuit potential (OCP) for 1 h. Next, the specimens were subjected to potentiodynamic polarization at a

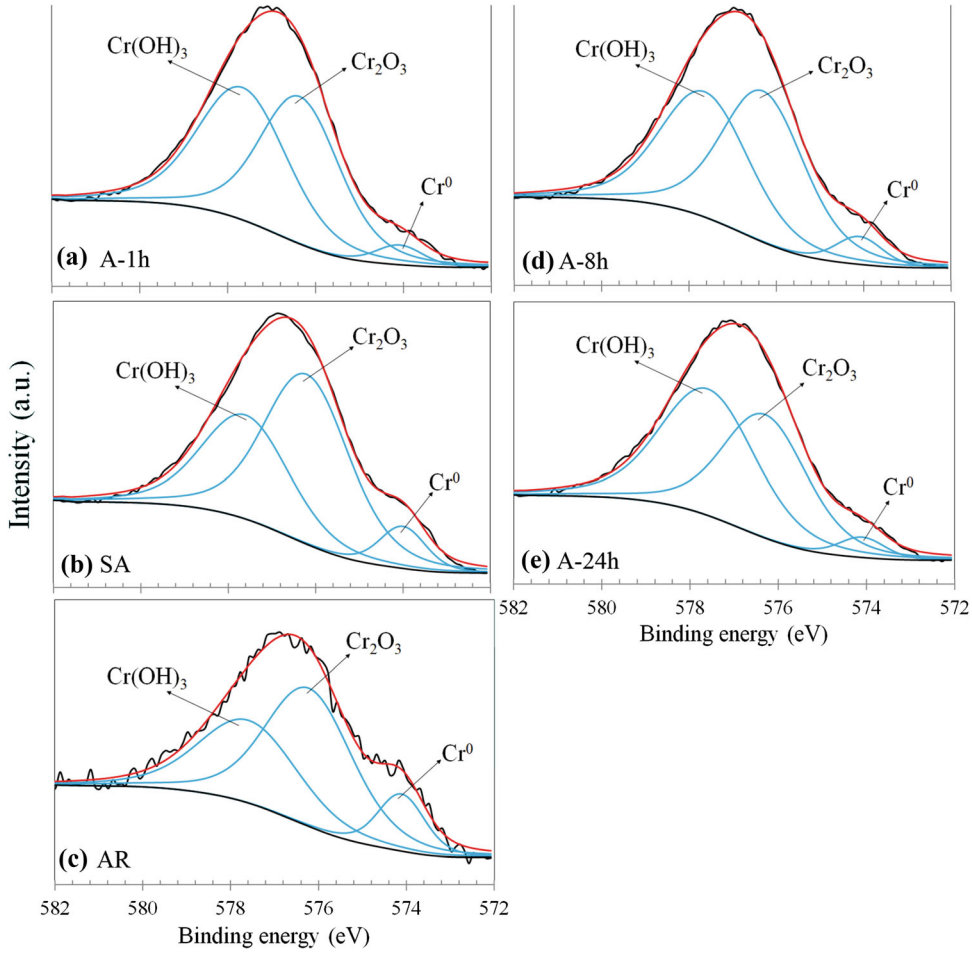

Fig. 2 XPS Cr2p3/2 spectra of the ASTM F-139 stainless steel samples: (a) A-1h; (b) SA; (c) AR; (d) A-8h; and (e) A-24h

sweep rate of 1 mV s^{-1} starting at − 300 mV versus the OCP up to + 1.0 $V_{Ag/AgCl}$. At least three different specimens were tested for each sample. The corrosion morphology after potentiodynamic polarization was examined by confocal laser scanning microscopy (CLSM, Olympus LEXT OLS4100).

Another set of experiments was conducted to evaluate the semiconducting properties of the passive film by the Mott–Schottky approach. In this case, the OCP was monitored for 600 s. Next, Mott–Schottky plots ($1/C^2$ vs. E) were acquired at a fixed frequency of 1 kHz in the potential range from 0.5 $V_{Ag/AgCl}$ up to − 1.0 $V_{Ag/AgCl}$ with a step of 25 mV in cathodic direction. The classic Mott–Schottky equation (Eq 1, p-type and Eq 2, n-type semiconductors) was employed to determine the acceptors (N_A) and donors (N_D) density of the passive film, assuming that the electrode capacitance is equal to the space charge capacitance at sufficiently high frequencies. In these equations, E is the applied potential, C is the space charge capacitance, k is the Boltzmann constant, T is the absolute temperature, e is electron charge (1.6×10^{-19} C), E_{FB} is the flat band potential, $\varepsilon = 12$ is the dielectric constant of the oxide film (Ref 19) and ε_0 is the vacuum permittivity (8.85×10^{-14} F/cm). The charge carrier densities (N_A and N_D) are determined from the slopes of the $1/C^2$ vs. E plots. A positive slope is related to n-type semiconducting behavior, whereas a negative slope denotes a p-type behavior. According to the literature, the passive films of stainless steels have a typical duplex character showing p-type and n-type responses depending on the potential range (Ref 20-22):

$$\frac{1}{C^2} = -\frac{2}{\varepsilon \cdot \varepsilon_0 \cdot e \cdot N_A}\left(E - E_{FB} - \frac{kT}{e}\right) \quad \text{(Eq 1)}$$

$$\frac{1}{C^2} = -\frac{2}{\varepsilon \cdot \varepsilon_0 \cdot e \cdot N_D}\left(E - E_{FB} - \frac{kT}{e}\right) \quad \text{(Eq 2)}$$

2.3 Microstructural Characterization

The microstructure of the AR and heat-treated samples was characterized by optical microscopy (Olympus LEXT OLS4100 confocal laser scanning microscope). The specimens were ground using SiC waterproof papers up to grit 2400, followed by mechanical polishing with diamond paste up to 1 µm. Electrolytic etching was, then, carried out in an oxalic acid solution (10 wt.%) at room temperature. The specimen was connected at the anode of a DC power supply. A stainless steel plate was used as cathode. The specimen was etched at 1 mA cm^{-2} for 90 s, according to the procedure described in ASTM A262-15. Next, the etched specimen was carefully removed from the electrolytic solution using stainless steel tweezers, washed with deionized water and dried using a heat gun. The grain size was determined based on ASTM E112-13.

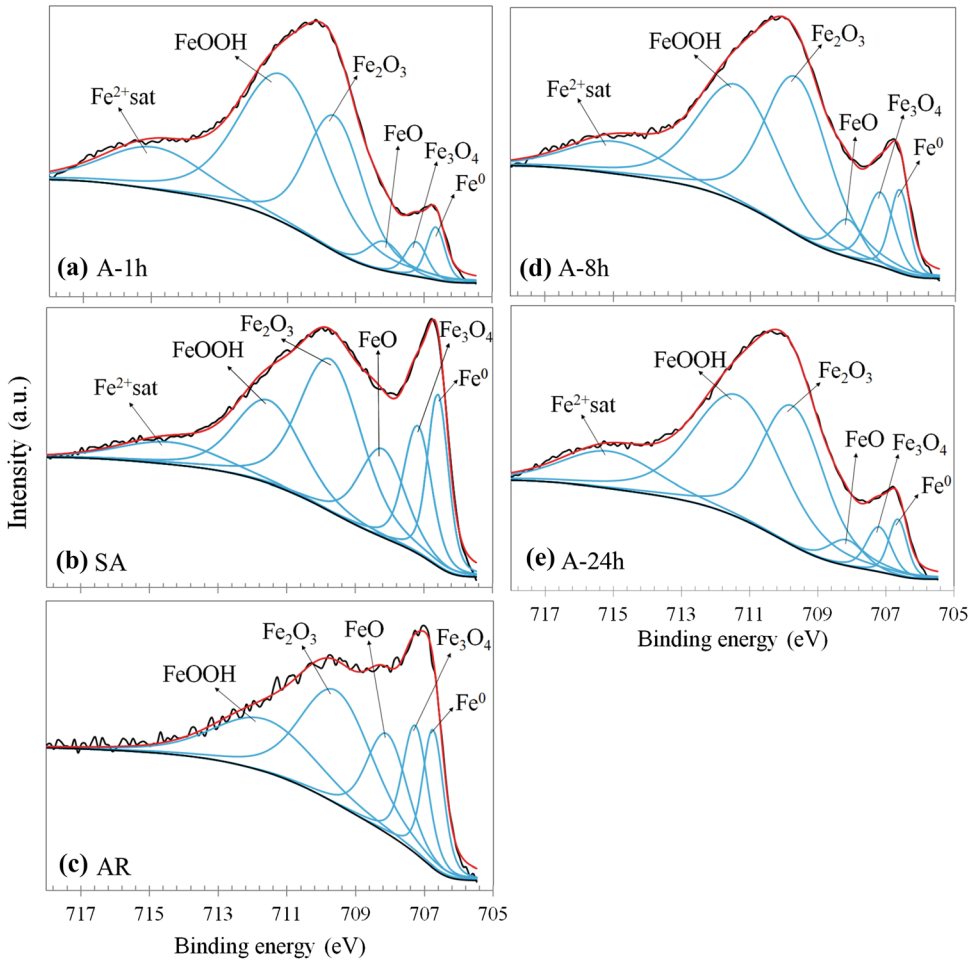

Fig. 3 XPS Fe $2p_{3/2}$ core levels of the ASTM F-139 stainless steel samples: (a) A-1h; (b) SA; (c) AR; (d) A-8h; and (e) A-24h

2.4 XPS Analysis

XPS analyses were conducted in a Thermo VG K-alpha^{+} spectrometer using Al-kα radiation source (1486.6 eV) and a spot size of 400 µm. Core levels for Fe 2p, Cr 2p, Ni 2p, Mo 3d and O 1s were fitted using a mixture of Gaussian–Lorentzian functions in the Avantage™ software and Smart algorithm for background subtraction. The binding energies were calibrated with respect to the C 1s peak at 284.8 eV (adventitious carbon). The pressure in the analysis chamber was approximately 10^{-7} Pa. Depth profile experiments were also conducted to assess the chemical composition of the passive film through its thickness. In this case, the surface was etched by medium-energy argon ions (Ar^{+}) until the passive film is removed.

3. Results

3.1 Microstructural Characterization

Figure 1 shows optical micrographs of the AR and heat-treated samples. A typical austenite microstructure with observable twins is recognized for all samples. The most striking feature is related to the grain size. The AR condition is the most refined one which is a must-attend feature of the ASTM F-139 standard in order to achieve high mechanical strength and suitable fatigue properties for biomedical applications. The SA and annealed materials microstructures presented a marked grain growth when compared to the AR condition. The grain sizes were determined based on ASTM E112-13. The results are displayed in Table 2. As can be seen, grain size increased more than 100% for the treated samples. If one considers the standard deviations, it is not possible to observe a significant effect of the annealing time on the grain size.

3.2 Chemical Composition of the Passive Film

3.2.1 XPS Core Levels. The chemical composition of the passive film was assessed by XPS analysis. High-resolution spectra were acquired for the Cr $2p_{3/2}$, Fe $2p_{3/2}$, Ni $2p_{3/2}$, Mo 3d and O 1s core levels. Figure 2 shows the Cr $2p_{3/2}$ high-resolution spectra for the AR and heat-treated samples. The spectra were fitted considering three different components, independently of the heat treatment condition. Metallic chromium (Cr^{0}) was detected at approximately 574 eV. The component at intermediate energies was assigned to Cr_2O_3, whereas $Cr(OH)_3$ appears at the highest binding energy. The positions of such species are in good agreement with other published data (Ref 23-25). The signal of metallic chromium was detected with a higher intensity on the surface of the AR sample. After heat treatment, it was still observed but at lower

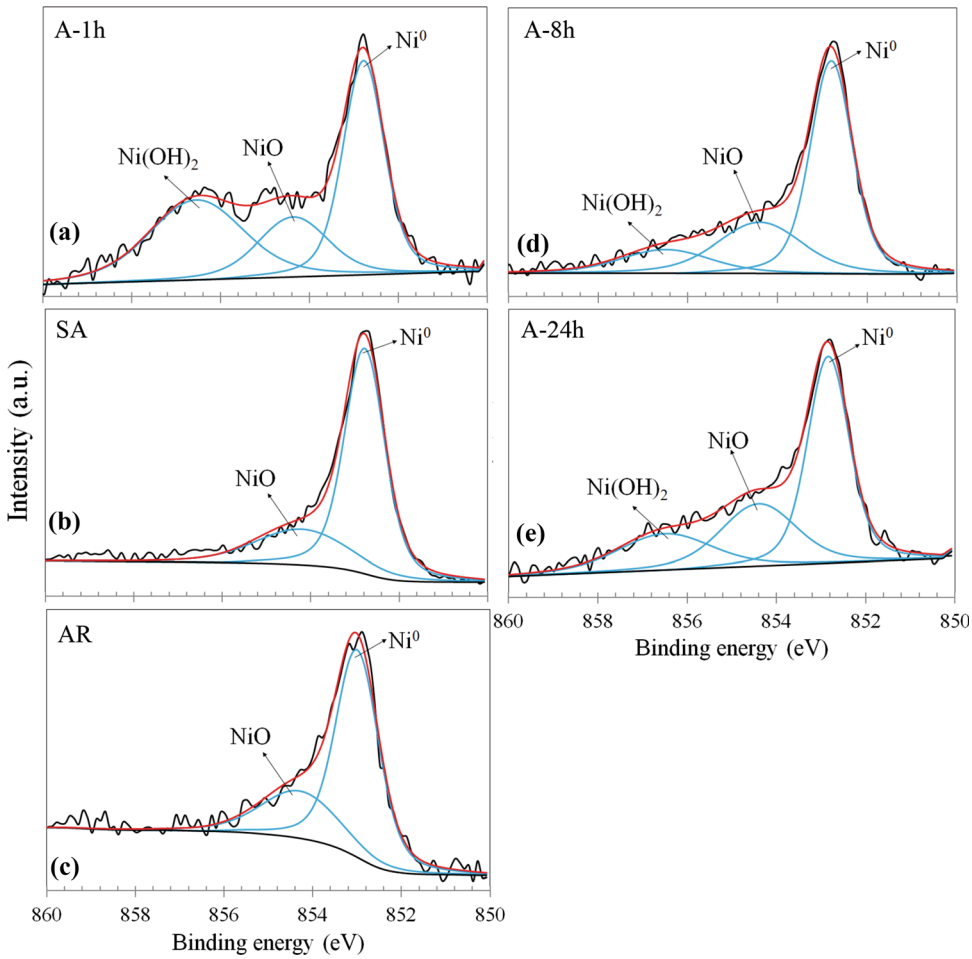

Fig. 4 XPS high-resolution spectra of the ASTM F-139 stainless steel samples in the Ni 2p3/2 region: (a) A-1h; (b) SA; (c) AR; (d) A-8h; and (e) A-24h

concentrations. The signal of the metallic species is associated with the steel substrate, as observed by other authors (Ref 26, 27). The main chromium species in the passive films are, therefore, Cr_2O_3 and $Cr(OH)_3$.

Iron was the other main constituent of the passive films on the ASTM F-139 samples. The iron species were assessed from Fe 2p core levels in the Fe $2p_{3/2}$ region, as shown in Fig. 3. Iron is present in five different chemical states. Metallic iron (Fe^0) appears as the lowest binding energy species. A mixture of Fe^{2+} and Fe^{3+} species is present in the passive film. Fe_3O_4, FeO, Fe_2O_3 and FeOOH were observed, in good agreement with the literature (Ref 28-30). These compounds are the main oxidized iron species for all samples, AR and heat treated. Moreover, a strong Fe^{2+} satellite peak is seen in the spectra of the heat-treated samples. It appears at approximately 715 eV, as reported by other authors (Ref 31, 32). The intensity of metallic iron signal decreased after heat treatment. This effect was more accentuated for the samples annealed at 700 °C after being solution-annealed at 1050 °C for 1 h. For these samples, the main oxidized iron species are FeOOH and Fe_2O_3. According to Zhang et al. (Ref 25), the stability of the passive film increases with the Fe^{3+}/Fe^{2+} ratio. It is, therefore, plausible to hypothesize that annealing at 700 °C could be beneficial to the protective character of the passive film of the ASTM F-139 samples, since it promoted an increase in the FeOOH and Fe_2O_3 (Fe^{3+} species) concentrations in the film. Additionally, it is reported that Fe^{3+} species enhance the n-type character of the oxide film, whereas Fe^{2+} are associated with p-type semiconducting behavior (Ref 33). As a consequence, the semiconducting character of the passive film may also be affected by the heat treatments which, in turn, may also influence its corrosion protection ability. These aspects will be discussed in the next sections.

Figure 4 shows the XPS high-resolution spectra in the Ni $2p_{3/2}$ region for the AR and heat-treated samples. In the AR condition, nickel exists primarily in the metallic state, as shown in Fig. 4(c). Only a weak NiO peak is observed. The same finding could be perceived in the SA sample, as shown in Fig. 4(b). By contrast, nickel hydroxide was unequivocally found as a third component in the spectra of the annealed samples (A-1h, A-8h and A-24h). Notwithstanding, in spite of the increase in fraction oxidized species, metallic nickel (Ni^0) is also the predominant constituent on the surface of the annealed samples. The peak positions are in good agreement with the literature (Ref 34, 35). The high concentration of the metallic species can be ascribed to the low oxygen affinity of nickel with respect to chromium and iron (Ref 36).

The Mo 3d core levels are shown in Fig. 5. The superposition of Mo species in the Mo $3d_{5/2}$ and Mo $3d_{3/2}$ levels is known to make deconvolution of Mo spectra a hard task, especially when the atomic concentrations of these species are low in the passive film, as is often reported (Ref 37, 38).

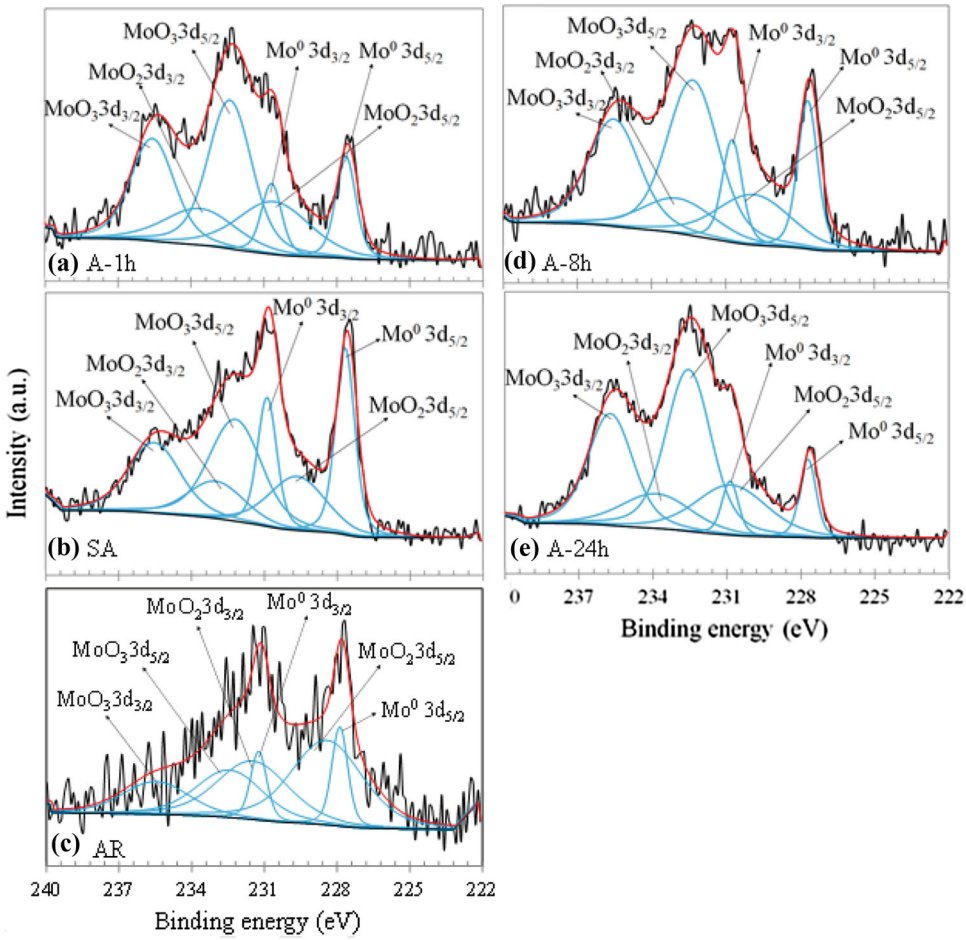

Fig. 5 XPS high-resolution spectra of the ASTM F-139 stainless steel samples in the Mo3d region: (a) A-1h; (b) SA; (c) AR; (d) A-8h; and (e) A-24h

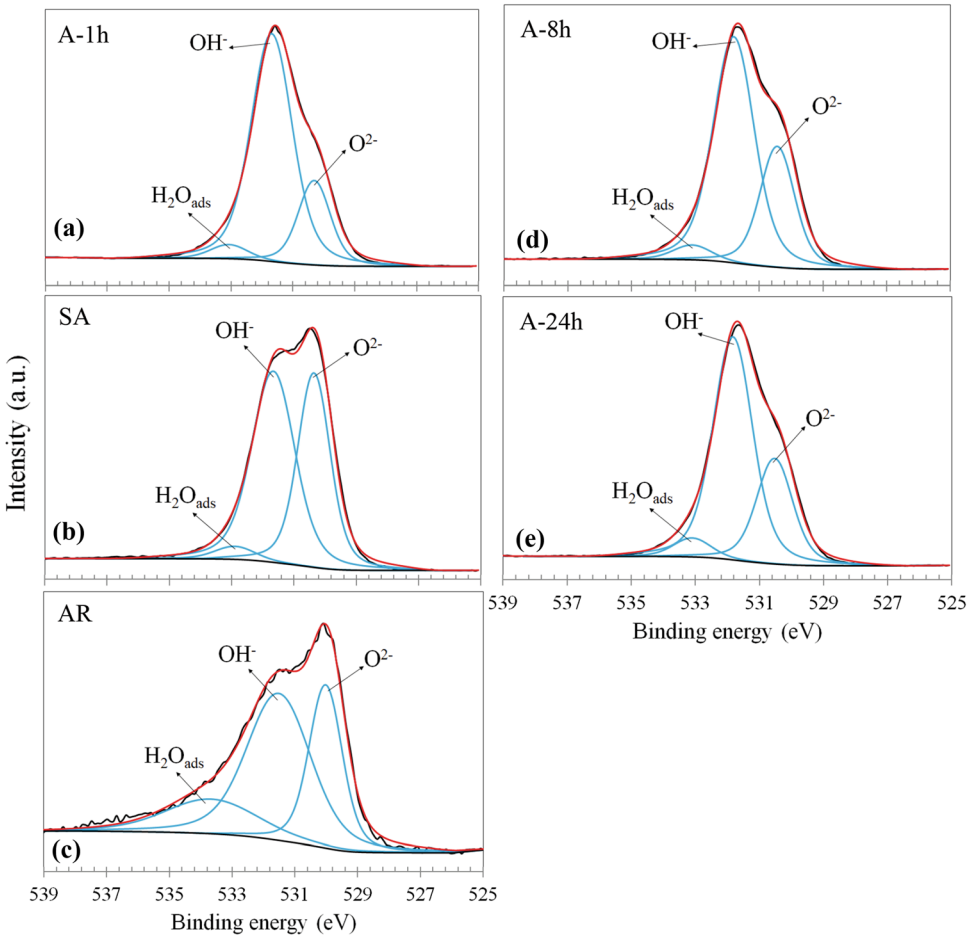

Fig. 6 XPS high-resolution spectra of the ASTM F-139 stainless steel samples in the O 1s region: (a) A-1h; (b) SA; (c) AR; (d) A-8h; and (e) A-24h

Notwithstanding, our data allowed clearly identifying different Mo species. The naturally formed passive film on the surface of the AR sample (Fig. 5c) presents Mo^{4+} (MoO_2) and Mo^{6+} species (MoO_3) along with detection of the metallic state. For all heat-treated samples, the same compounds were found. Peak positions are in good agreement with other published data (Ref 39-41).

O 1s spectra of ASTM F-139 stainless steel in the AR and heat-treated conditions are displayed in Fig. 6. The spectra were split into three components. Oxide species are related to O^{2-} bonds at approximately 530 eV. Hydroxides (OH^- bonds) appear at intermediate frequencies near 531 eV, whereas bound water was found as the highest binding energy component at 533 eV. Similar results were reported by other authors for the passive films on 316L-type stainless steels (Ref 42-44). Oxide species predominate over hydroxides after annealing (samples A-1h, A-8h and A-24h). Moreover, it is noteworthy that the passive film becomes less hydrated for the heat-treated samples when compared to the material in the as-received condition (AR), as indicated by the lower intensity of the peak associated with adsorbed water.

3.2.2 Depth Profile Experiments. The constitution of the passive films formed on the ASTM F-139 stainless steel in the AR and heat-treated conditions was further assessed by depth profile experiments through the thickness of surface oxides. The results are shown in Fig. 7.

The main elements that constitute the ASTM F-139 stainless steel are detected in the passive films of all samples. The nickel and molybdenum signals are very low in the beginning of the experiment, increasing through the thickness of the passive layer until reaching a roughly constant concentration as it is removed by exposure to the argon ions flux. It is interesting to note that the AR condition is richer in iron species than the heat-treated samples in the first cycle. Iron is more easily oxidized than Cr, Ni and Mo, being the major constituent of the passive film for all samples, as observed by other authors (Ref 45). The concentrations of all species follow a similar trend, independently of the heat treatment condition. Chromium is enriched in the inner part of the passive film with respect to the surface. Nickel and molybdenum present the same trend.

In order to achieve a more detailed picture of the composition of the passive films and eventual differences arising from the heat treatments, the Cr/Fe and Mo/Fe ratios of all samples were calculated from the depth profile data. The results are shown in Fig. 8.

The Cr/Fe ratio of the heat-treated samples is higher than that of the naturally formed passive film in the AR surface, especially from 40 s up to 200 s. It is not possible, though, to

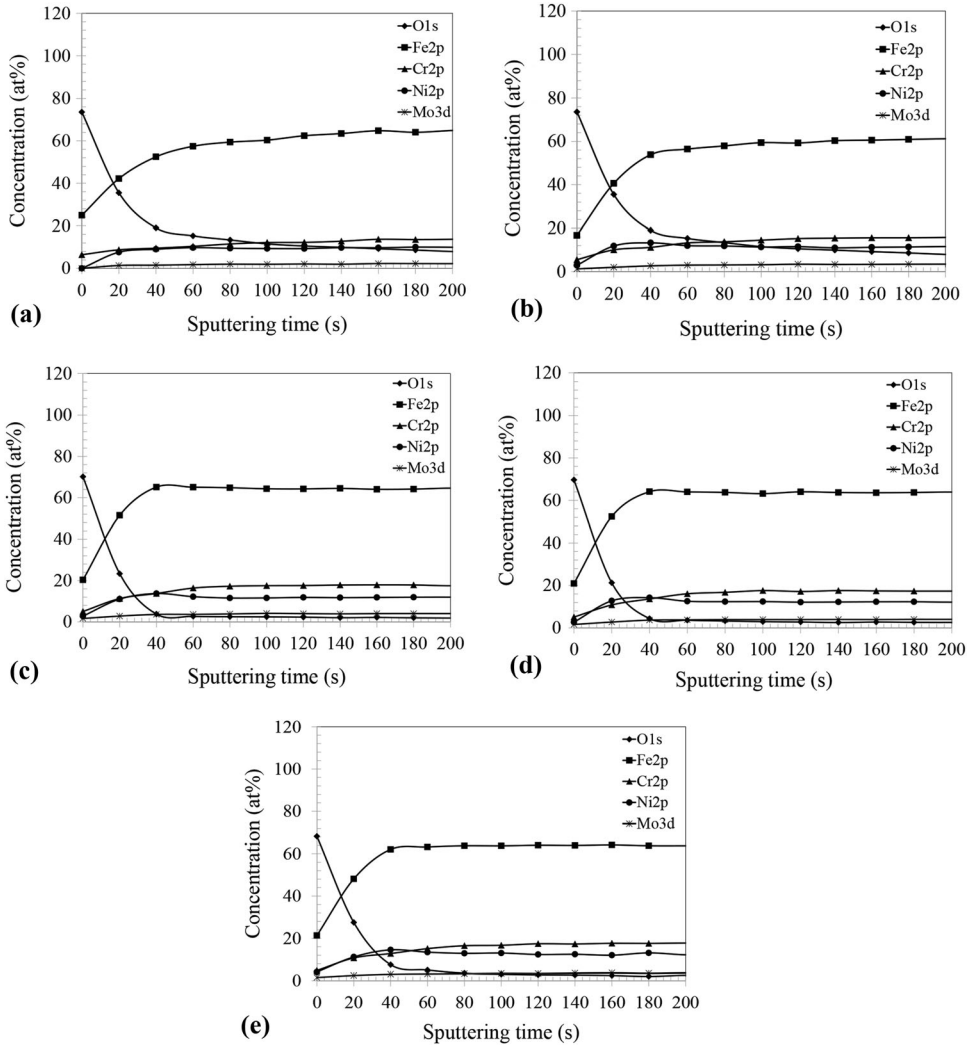

Fig. 7 XPS depth profiles of the ASTM F-139 stainless steel: (a) AR; (b) SA; (c) A-1h; (d) A-8h; (e) A-24h

observe significant differences between them, especially for the annealed samples (A-1h, A-8h and A-24h). Mo/Fe ratio shows a marked difference between the AR and heat-treated samples throughout the whole sputtering range. Indeed, it is noteworthy that the Mo concentration is negligible at the initial step for the AR condition and is lower than the treated surfaces over the whole experiment. In spite of the similarity of the Mo/Fe ratio between the heat-treated samples, it is slightly higher for the A-1h and A-8h conditions, indicating a passive film richer in Mo when compared to the other samples.

3.3 Electrochemical Tests

3.3.1 Potentiodynamic Polarization. Figure 9 shows the potentiodynamic polarization curves for the AR and heat-treated ASTM F-139 stainless steel samples. The results were obtained after 1 h of immersion in PBS solution at 37 °C. The values of corrosion potential (E_{corr}), passive current density (i_{pass}), breakdown potential (E_b) and passive range ($\Delta E = E_b - E_{corr}$) were determined from these curves. The values of i_{pass} were determined at the middle of the passive range. The data are shown in Table 3.

The lowest i_{pass} was obtained for the sample annealed for 8 h, indicating its slower dissolution kinetics when compared to the other samples. Additionally, it also presents the highest value of breakdown potential (E_b) and widest passive range (ΔE), revealing reduced pitting corrosion susceptibility. Its corrosion potential (E_{corr}) is shifted in the anodic direction with respect to the as-received alloy and the other heat-treated conditions, confirming the more stable character of its passive film. A similar trend was observed for the A-1h. However, the shift of E_{corr} into the anodic direction was not as marked as that of A-8h and the passive range was only slightly extended when compared to the as-received condition.

There was also an increase of the passive range for the sample A-24h in comparison with the as-received condition. However, it was much smaller than was observed for the A-8h sample. Notwithstanding, the E_b value of the A-24h is lower than that of the AR and its E_{corr} is shifted to a more negative value, suggesting its passive film is not as stable as that obtained for the sample annealed for 8 h. Solution annealing, in turn, seems to have only little influence on the corrosion properties and stability of the passive film of the ASTM F-139 stainless steel, since the values of E_{corr}, E_b and ΔE are little altered with respect to the as-received alloy.

The corrosion morphology of the AR and heat-treated samples after potentiodynamic polarization was examined

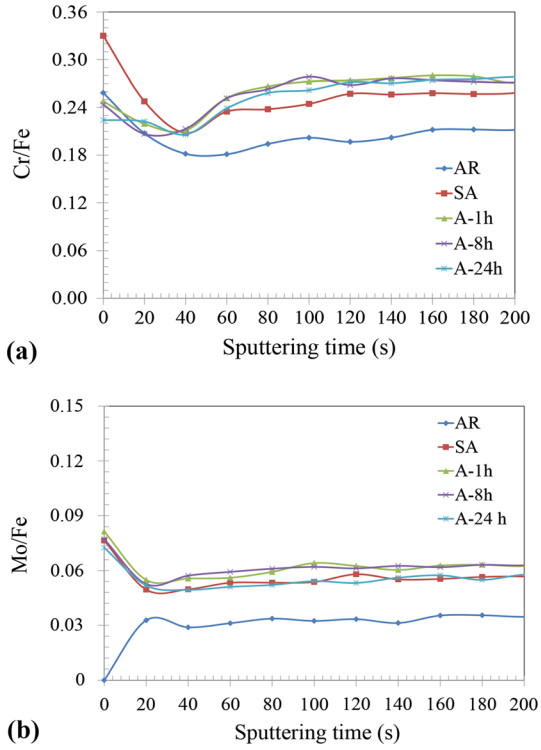

Fig. 8 (a) Cr/Fe and (b) Mo/Fe ratios obtained from the XPS depth profile experiments

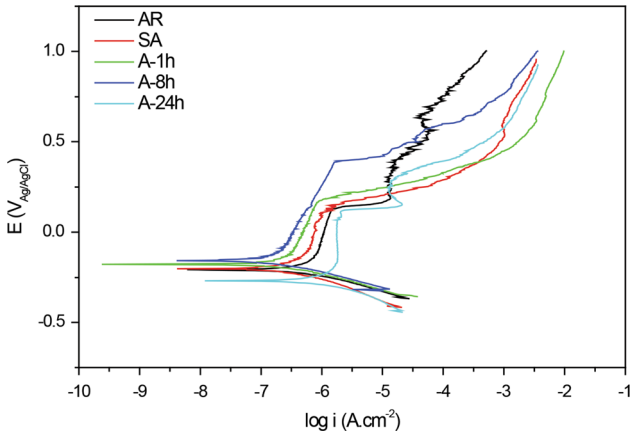

Fig. 9 Potentiodynamic polarization curves of the AR and heat-treated ASTM F-139 stainless steel samples after immersion in PBS solution for 1 h at 37 °C

Table 3 Electrochemical parameters determined from the potentiodynamic polarization curves shown in Fig. 9

Sample	i_{pass}, μA cm^{-2}	E_{corr}, mV$_{Ag/AgCl}$	E_p, mV$_{Ag/AgCl}$	ΔE, mV
AR	1.10	− 202	138	340
SA	0.79	− 204	141	345
A-1h	0.44	− 180	176	356
A-8h	0.39	− 158	390	548
A-24h	1.78	− 245	120	365

using CLSM. The micrographs are displayed in Fig. 10. Pits were clearly visible in the AR (Fig. 10a) and A-24h (Fig. 10e) samples. Smaller pits appeared in the solution-annealed sample (Fig. 10b). Fewer pits were observed in the A-1h sample (Fig. 10c). As the A-8h condition presented the highest pitting corrosion resistance, only very small pits were found, as pointed by the circle in Fig. 10(d).

3.3.2 Semiconducting Properties of the Passive Film. Further insights into the understanding of the effect of the heat treatments on the passive film stability of the ASTM F-139 stainless steel were provided by the Mott–Schottky plots shown in Fig. 11. The results were obtained after immersion in PBS solution at 37 °C for 1 h. The acceptors (N_A) and donors (N_D) densities were determined from the linear portions of these plots based on Eq. 1 and 2, respectively. The data are shown in Table 4.

Independently of the heat treatment condition, all the samples presented a duplex character, as denoted by the positive slopes for potentials below − 0.13 $V_{Ag/AgCl}$ and negative slopes above it. The negative slopes are associated with a typical p-type semiconducting behavior for which the main defects are cation vacancies (Ref 46). The positive slopes indicate an n-type semiconducting character which is due to the predominance of defects such as cation interstitials and oxygen vacancies in the passive film (Ref 47). The point defect model (PDM) (Ref 48) postulates that chloride ions are likely to occupy the oxygen vacancies in the passive film. This absorption process is autocatalytic, enabling an enhancement in the flux of cation vacancies into the interface between the metal substrate and the passive film. The cation vacancies are annihilated by the metal ions released during oxidation. Accumulation of cation vacancies is expected at the passive film if this reaction is slow, leading to its condensation and, consequently, forming voids that make the passive layer thinner and less protective against dissolution (Ref 49). It is, therefore, expected that passive films with higher donor densities (N_D) would be more prone to pitting corrosion (Ref 50). High density of point defects implies in a high conductive passive film (Ref 51), affecting its corrosion protection ability.

The data shown in Table 4 clearly indicate that the passive film formed on the surface of the A-8h sample presents few defects which is consistent with the high pitting corrosion resistance observed in the potentiodynamic polarization curves (Fig. 9). The AR and A-24h samples, in turn, presented the highest N_A and N_D values. The low stability of the passive films formed on these samples can be associated with their high densities of point defects (oxygen vacancies, cation interstitials and cation vacancies).

4. Discussion

The corrosion resistance of the ASTM F-139 stainless steel was affected by the heat treatment condition, as depicted in section 3.3.1. The microstructures of the heat-treated samples were characterized, and an increase in the grain size was observed (section 3.1). Such grain growth should be considered for actual applications of the ASTM F-139 with regard to its possible effect in its mechanical properties. According to ASTM F-139 requirements, the material should present an average grain size of 63.5 μm (ASTM grain size number 5) or

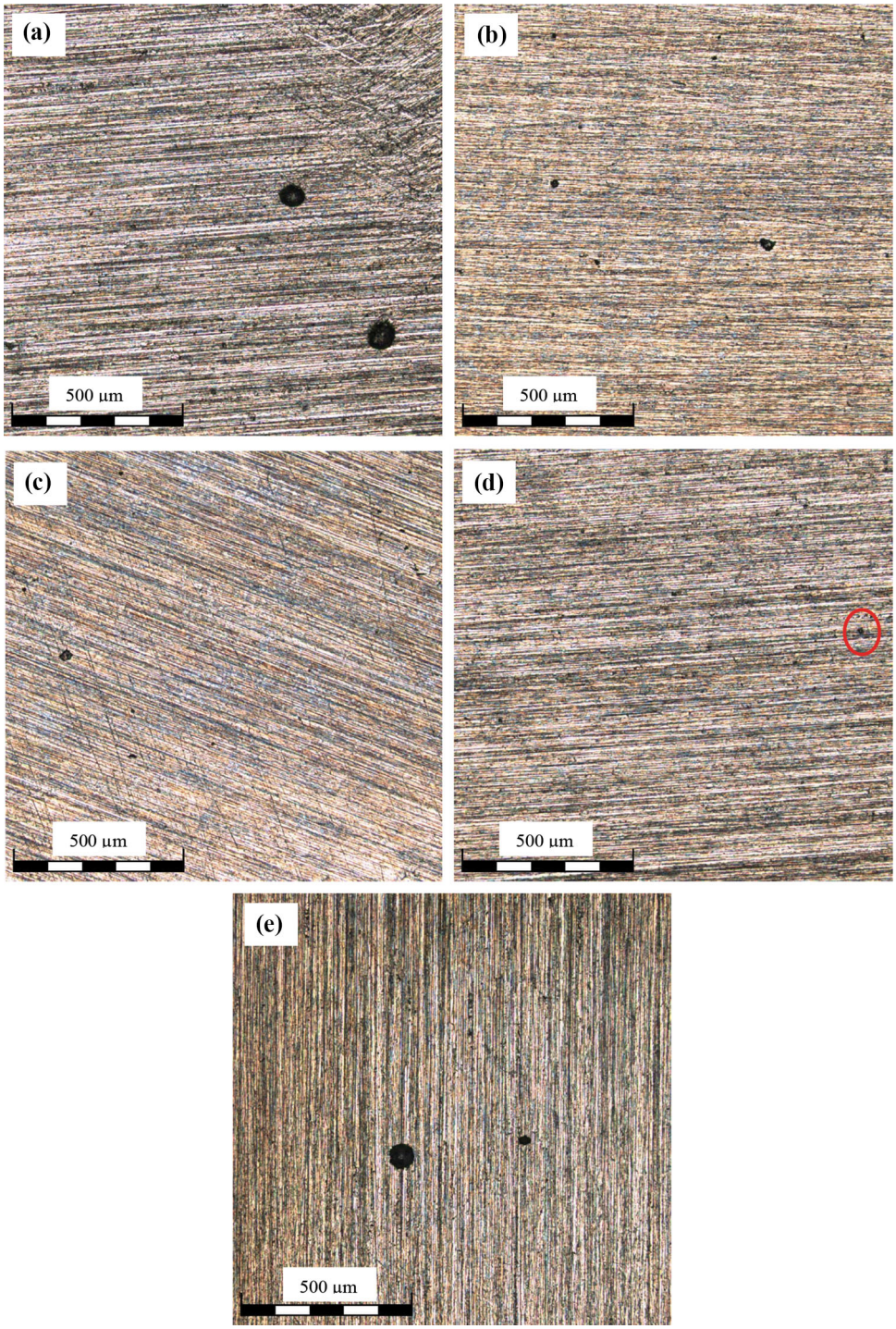

Fig. 10 Optical micrographs of the AR and heat-treated ASTM F-139 stainless steel samples after potentiodynamic polarization: (a) AR; (b) SA; (c) A-1h; (d) A-8h; (e) A-24h

finer. In this respect, even the longest annealing treatment (24 h) yielded a microstructure within the limits of the standard and should not prevent its use for possible control of the passive film composition. It is important to realize that, in spite of a general increasing trend of the grain size with the annealing time, it was not possible to observe significant differences between the grain sizes of the samples, if one considers the standard deviations, as shown in Table 2. The corrosion behavior should be, therefore, controlled by other factors. In order to clarify this issue, the surface chemistry and semiconducting properties of the passive films were assessed.

At a first glance, the surface chemistry of the passive film was not significantly influenced by the heat treatment condition, since its chemical composition was not altered, according to the XPS high-resolution spectra shown in section 3.2.1. Independently of the annealing time, the same species were found in the passive films which were mainly composed of a mixture of chromium and iron oxides and hydroxides with

minor fractions of nickel oxide and hydroxide and molybdenum oxides. The main differences were observed for the nickel and molybdenum species. Whereas nickel oxide was the only oxidized nickel species on the AR and SA samples, the annealed samples presented also nickel hydroxide on its surface layer. The only oxidized molybdenum species in the passive film of the AR sample was MoO_2, while all heat-treated samples presented also Mo^{6+} species in the passive film (MoO_3). None of these characteristics, though, can be correlated with the corrosion properties described in section 3.3.2.

The depth profiles (section 3.2.2), in turn, indicated noticeable compositional differences between the samples, especially with respect to the Mo/Fe ratio that was higher for the A-1h and A-8h. It is important, therefore, to assess the depth profile results with more detail in order to obtain additional information on the chemical composition of the passive film through its thickness. With this idea borne in mind, peak deconvolution of the Cr $2p_{3/2}$, Mo3d and Fe $2p_{3/2}$ spectra was undertaken for selected sputtering times up to 100 s for which the passive film of all samples was mostly removed, as suggested by the depth profile shown in Fig. 7.

Figure 12 displays the relative concentration of the chromium species in the passive films of the AR and heat-treated ASTM F-139 stainless steel samples for selected sputtering times during XPS depth profile analysis. Some interesting features can be highlighted from these data. Chromium hydroxide ($Cr(OH)_3$) is the main oxidized chromium species on the surface (sputtering time at 0 s) of the naturally formed passive film on the AR sample (Fig. 12a), whereas chromium oxide (Cr_2O_3) predominates on the heat-treated samples at the same time. Moreover, Cr_2O_3 is enriched in the passive film of the A-8h sample (Fig. 12d) up to 100 s when compared to the other heat-treated samples. Chromium hydroxide is reported to present a lower protective character than chromium oxide, making the passive film stainless steels less stable in chloride-containing electrolytes (Ref 52, 53). The high pitting corrosion resistance of the A-8h sample (Fig. 9) could be due to its Cr_2O_3-rich passive film, whereas the higher pitting susceptibility of the AR condition would be related to its $Cr(OH)_3$-rich film. It is important to realize, though, that the concentrations of $Cr(OH)_3$ and Cr_2O_3 are not remarkably different for the A-8h and A-24h (Fig. 12e) samples, but their localized corrosion resistance is quite different as shown in Table 3.

Hence, it is likely that other factors may influence the pitting corrosion behavior of the heat-treated material. In addition to chromium, molybdenum plays also a central role in the passive film stability of stainless steels (Ref 54). We have, therefore, deconvoluted the Mo3d peaks of the AR and heat-treated samples for selected sputtering times. The relative concentrations of the molybdenum species are shown in Fig. 13. The surface of the passive films (at 0 s) is richer in MoO_3 species for the A-8h sample (Fig. 13d) when compared to the other samples. Similar contents of MoO_2 and MoO_3 were found for the annealed samples for longer sputtering times. These species are often reported to be part of the passive films of stainless steels, which are associated with their corrosion resistance (Ref 54, 55).

In fact, several authors (Ref 24, 56) have found that molybdenum does not present a significant effect on the composition of the passive films of stainless steels. Its major effect is centered in its ionic selectivity when present on the outer part of the passive film where it can act as an electron acceptor, enhancing the formation of Cr_2O_3 by creating more oxygen vacancies in the inner part of the passive layer (Ref 57). This effect is mainly due to Mo^{6+} species that are preferentially concentrated in the outer part of the passive film (Ref 58). Our results also point to this direction, since MoO_3 signal is higher at the surface and disappears after 40 s for all annealed samples. Since the MoO_3 signal is more intense in the outer part of the passive film of the A-8h sample, it is likely that it could more effectively enhance the stability of the passive film against pitting corrosion, by enhancing the formation of an enriched Cr_2O_3 layer. This would support the findings of the potentiodynamic polarization tests described in section 3.3.1.

Additional support to the above-discussed effects of the chromium and molybdenum species in the passive film composition and corrosion stability can be provided by the analysis of the Fe $2p_{3/2}$ spectra at selected sputtering times during the XPS depth profile experiments. The results are shown in Fig. 14. The hydrated nature of the passive film is related to the presence of hydroxide species, such as FeOOH which are reported to form porous, non-protective layers against corrosion (Ref 59). These species are likely to be encountered in the outer part of the passive film. Indeed, our results indicate that FeOOH was only found in the outer part of the passive films of the heat-treated samples, whereas it spread through the passive film thickness only for the as-received material (Fig. 14a). The only two samples for which the FeOOH species is completely removed after only 20 s of sputtering (1 cycle) were the A-1h and A-8h, indicating it is only present at the outer part of the passive films. As the sputtering time increases, iron oxides predominate and become the unique oxidized iron species, such as Fe_3O_4, FeO and Fe_2O_3 for all heat-treated samples. The A-8h sample shows another distinct aspect that is not found in the other heat-treated samples. Its FeO concentration is high from 20 s up to 100 s of sputtering, remaining rather homogeneous throughout the thickness of the passive film and overcoming all other samples. According to the literature (Ref 60, 61), Fe^{2+} oxides are more corrosion resistant than Fe^{3+}-based ones. It is expected, therefore, that passive films rich in FeO should present higher resistance to pitting corrosion. In this regard, the passive film stability of the A-8h sample would be favored, since it presented high concentration and homogeneous distribution of FeO throughout its thickness (Fig. 14d).

The detailed assessment of the XPS depth profiling data gave important information about the relationship between the chemical composition of the passive films formed on the AR

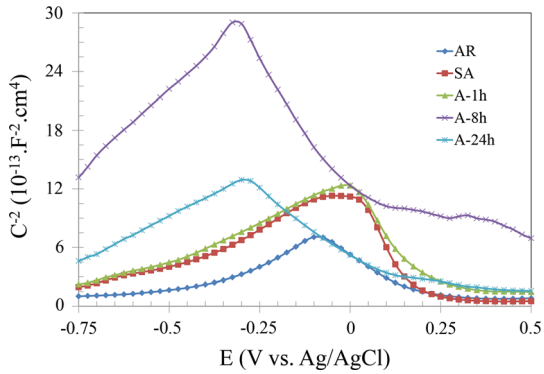

Fig. 11 Mott–Schottky plots of the AR and heat-treated samples after 1 h of immersion in PBS solution at 37 °C

and heat-treated samples and its corrosion resistance. The passive film of the A-8h is enriched with MoO_3, Cr_2O_3 and FeO which is considered to be the main responsible for its high corrosion stability when compared to the other samples. As well established in the literature, the semiconducting properties of the passive film are also intimately related to its pitting corrosion susceptibility (Ref 62).

As shown in Fig. 11 (section 3.3.2), the passive films of all samples presented two linear portions, revealing its duplex character which is associated the transition from n-type (positive slope) to p-type (negative) semiconducting behavior. It is well documented that Cr_2O_3 behaves as a p-type semiconductor, whereas iron oxides/hydroxides present n-type behavior (Ref 63, 64). Moreover, MoO_3 is reported to behave as n-type semiconductor, whereas MoO_2 presents a p-type character (Ref 65). Both species, although in minor concentrations when compared to Fe and Cr compounds, were detected on the surface films of the AR and heat-treated samples. In this respect, the mixed composition of the passive films of all samples as determined by XPS analyses is likely to be responsible for the duplex semiconducting behavior. The p-type behavior is associated with an excess of cation vacancies or depletion of metal cations. The n-type character arises from cation transport promoted by interstitial diffusion or anion diffusion through the passive film into the metal/electrolyte interface (Ref 63).

According to Ningshen et al. (Ref 63), the dopants of passive films are the point defects themselves. Thus, lower values of doping densities, either acceptors (N_A) or donors (N_D), are related to an increasing resistance to pitting corrosion due to the less defective nature of the oxide layer. Conversely, when N_A and N_D are high, the passive film presents a marked

Table 4 Acceptors (N_A) and donors (N_D) densities determined from the Mott–Schottky plots shown in Fig. 11

Sample	N_A ($10^{16} \times cm^{-3}$)	N_D ($10^{16} \times cm^{-3}$)
AR	4.87	5.52
SA	1.72	5.51
A-1h	1.98	6.50
A-8h	1.91	3.38
A-24h	4.50	6.25

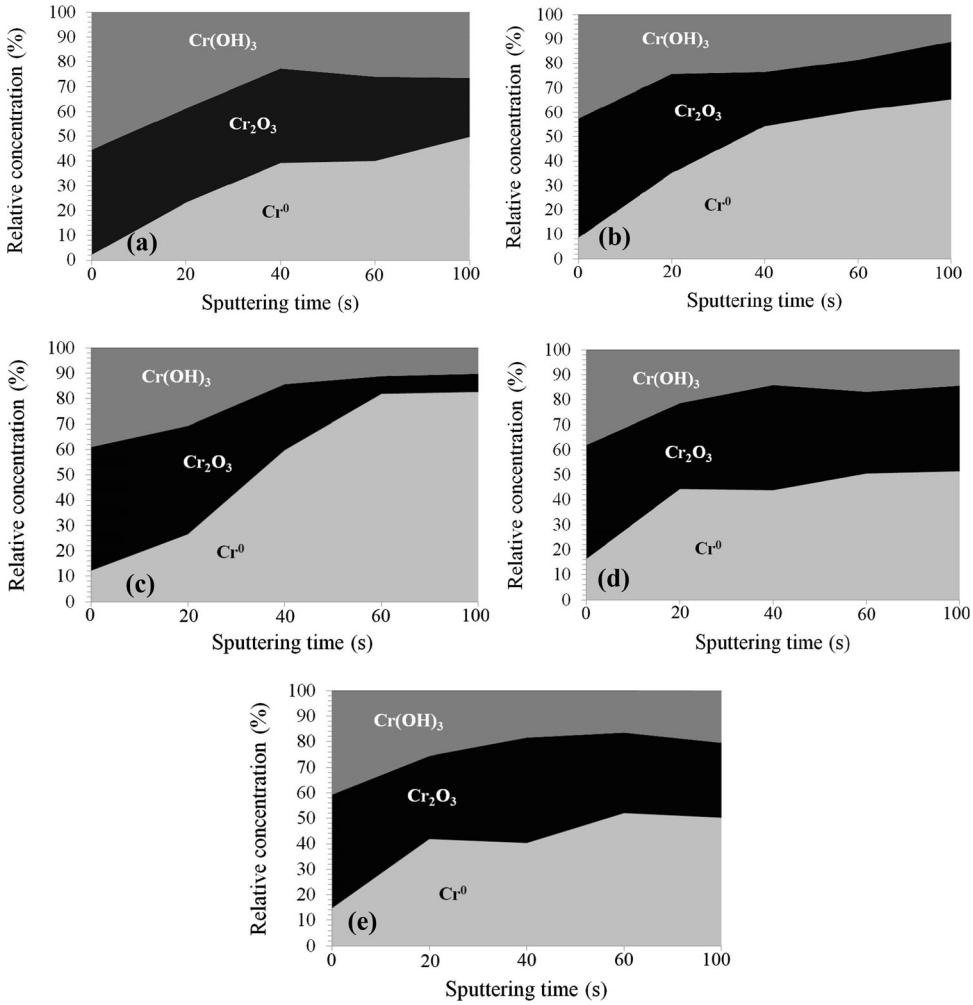

Fig. 12 Relative concentration of the chromium species in the passive films of the ASTM F-139 stainless steel samples obtained by peak deconvolution of the XPS spectra at selected sputtering times: (a) AR; (b) SA; (c) A-1h; (d) A-8h; and (e) A-24 h

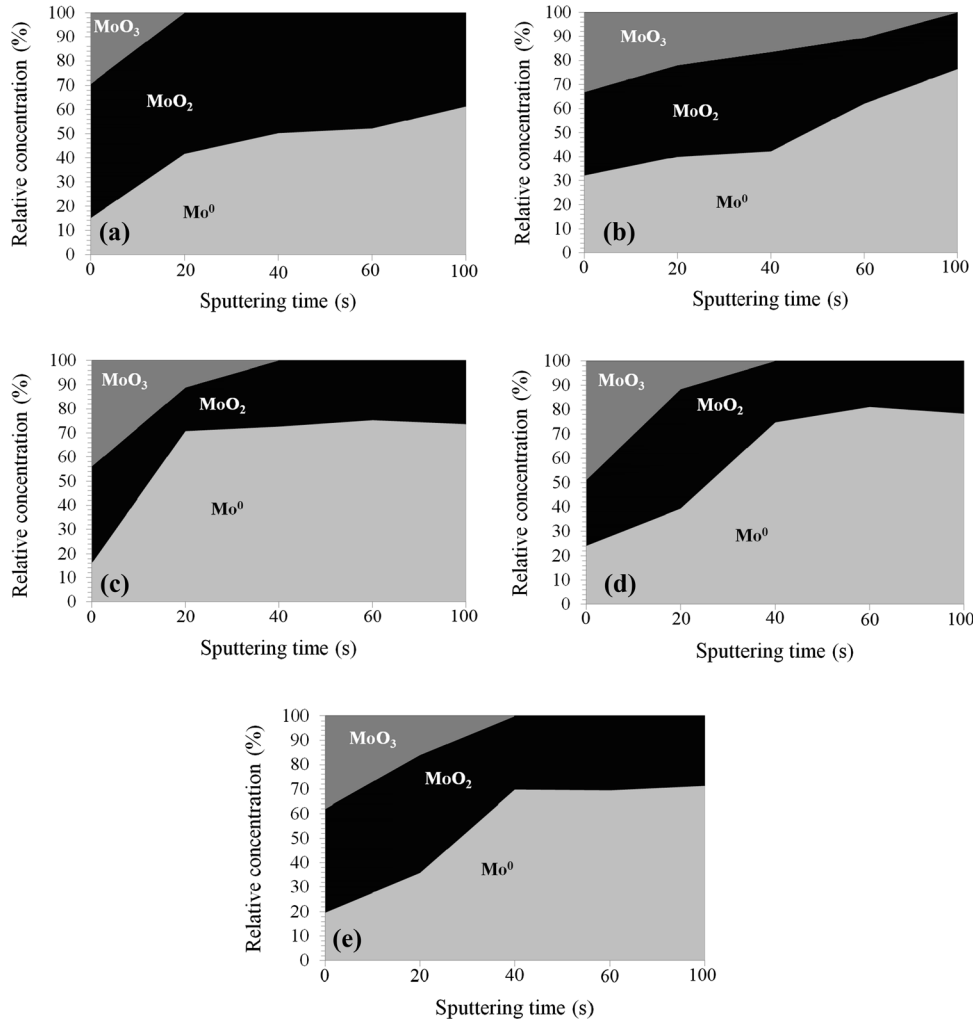

Fig. 13 Relative concentration of the molybdenum species in the passive films of the ASTM F-139 stainless steel samples obtained by peak deconvolution of the XPS spectra at selected sputtering times: (a) AR; (b) SA; (c) A-1h; (d) A-8h; and (e) A-24h

disordered character that hampers its corrosion protective ability (Ref 66). It is important to realize, hence, that the low N_A and N_D values of the A-8h sample (Table 4) reflect the formation of a passive film with fewer point defects and less disordered structure. As a consequence, the transport of chloride ions from the electrolyte would be less effective than for the other samples, thus leading to an increase in the pitting corrosion resistance.

Our results unequivocally show that the composition, electronic properties and corrosion resistance of the passive films formed on the ASTM F-139 stainless steel are correlated and depended on the heat treatment condition. One should not rule out its influence on the pitting corrosion susceptibility of the devices manufactured from this material. Specific conditions can be tailored to obtain optimized corrosion resistance.

5. Conclusions

The grain size of the ASTM F-139 stainless steel samples increased after heat treatment but was not significantly affected by the annealing condition. Its effect on the corrosion resistance of the alloy was considered to be negligible. The composition of the passive film, in turn, was affected by the heat treatment condition. The results obtained by XPS revealed enrichment in

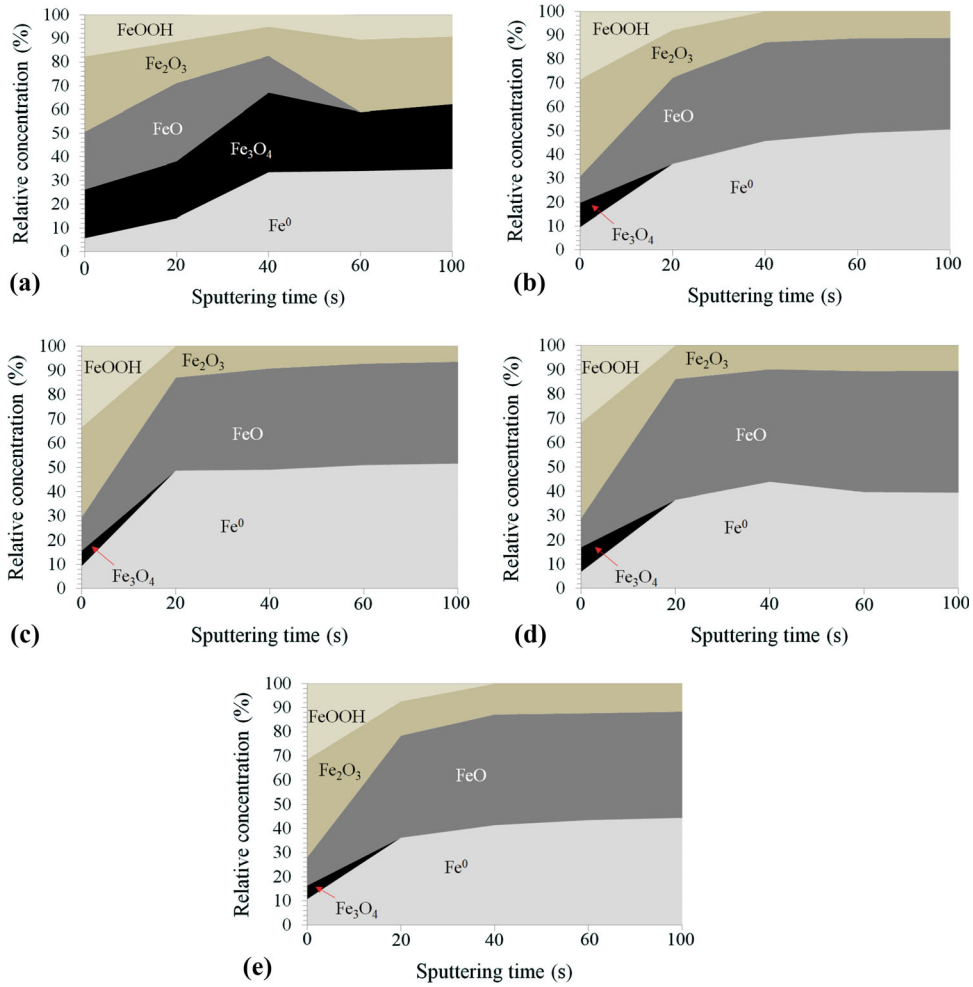

Fig. 14 Relative concentration of the iron species in the passive films of the ASTM F-139 stainless steel samples obtained by peak deconvolution of the XPS spectra at selected sputtering times: (a) AR; (b) SA; (c) A-1h; (d) A-8h; and (e) A-24h

Cr_2O_3, MoO_3 and FeO for the passive film obtained after an 8-h annealing period. Furthermore, the electronic properties of the passive films were also dependent on the heat treatment procedure. Annealing for 8 h promoted the formation of a less disordered oxide film. As a consequence of the compositional changes and alterations of the semiconducting properties of the passive films, the pitting corrosion susceptibility was decreased for the samples annealed for 8 h which presented a wide passive range and high breakdown potential.

Acknowledgments

The Multiuser Experimental Facilities (CEM-UFABC) are acknowledged for the experimental support to this work.

References

1. K. Prasad, O. Bazala, M. Chua, M. Rochford, L. Fedrick, J. Spoor, R. Symes, M. Tieppo, C. Collins, A. Cao, D. Markwell, K. Ostrikov, and K. Bazaka, Metallic Biomaterials: Current Challenges and Opportunities, *Materials*, 2017, **10**, p 884-1–884-33
2. N. Eliaz, Corrosion of Metallic Biomaterials: A Review, *Materials*, 2019, **12**, p 407-1–407-91
3. E.F. Pieretti, S.M. Manhabosco, L.F.P. Dick, S. Hinder, and I. Costa, Localized Corrosion Evaluation of the ASTM F139 Stainless Steel Marked by Laser Using Scanning Vibrating Electrode Technique, X-Ray Photoelectron Spectroscopy and Mott-Schottky Techniques, *Electrochem. Acta*, 2014, **124**, p 150–155
4. M.D. Pereda, K.W. Kang, R. Bonetto, C. Llorente, P. Bilmes, and C. Gervasi, Impact of Surface Treatment on the Corrosion Resistance of ASTM F138-F139 Stainless Steel for Biomedical Applications, *Proc. Mater. Sci.*, 2012, **1**, p 446–453
5. N. Hassan and N.A.A. Ghany, Corrosion of Biomaterials: Anodic Treatment and Evaluation of 316L Stainless Steel in Simulated Body Fluid, *Corros. Eng. Sci. Technol.*, 2017, **52**, p 267–275
6. K. Rokosz and T. Hryniewicz, Pitting Corrosion Resistance of AISI, 316L Stainless Steel in Ringer's Solution After Magnetoelectrochemical Polishing, *Corrosion*, 2010, **66**, p 035004-1–035004-11
7. P. Guzmán, W. Aperador, and L. Yate, Enhancement of the Pitting Corrosion Resistance of AISI, 316LVM Steel with Ta-Hf-C/Au Bilayers for Biomedical Applications, *J. Nanomater.*, 2017, **2017**, p 6825250-1–6825250-10
8. A. Bekmurzayeva, W.J. Duncanson, H.S. Azevedo, and D. Kanayeva, Surface Modification of Stainless Steel for Biomedical Applications: Revisiting a Century-Old Material, *Mater. Sci. Eng. C*, 2018, **93**, p 1073–1089
9. M. Talha, C.K. Behera, and O.P. Sinha, A Review on Nickel-Free Nitrogen Containing Austenitic Stainless Steels for Biomedical Applications, *Mater. Sci. Eng. C*, 2013, **33**, p 3563–3575
10. V. Azar, B. Hashemi, and M.R. Yazdi, The Effect of Shot Peening on Fatigue and Corrosion Behavior of 316L Stainless Steel in Ringer's Solution, *Surf. Coat. Technol.*, 2010, **204**, p 3546–3551

11. B. Deng, Y.M. Jiang, J. Gao, and J. Li, Effect of Annealing Treatment on Microstructure Evolution and the Associated Corrosion Behavior of a Super-Duplex Stainless Steel, *J. Alloys Compd.*, 2010, **403**, p 461–464
12. H. Tan, Y. Jiang, B. Deng, T. Sun, J. Xu, and J. Li, Effect of Annealing Temperature on the Pitting Corrosion Resistance of Super Duplex Stainless Steel UNS S32750, *Mater. Charact.*, 2009, **60**, p 1049–1054
13. A.A. Aghuy, M. Zakeri, M.H. Moayed, and M. Mazinani, Effect of Grain Size on Pitting Corrosion of 304L Austenitic Stainless Steel, *Corros. Sci.*, 2015, **94**, p 368–376
14. C. Bitondo, A. Bossio, T. Monetta, M. Curioni, and F. Bellucci, The effect of Annealing on the Corrosion Behaviour of 444 Stainless Steel for Drinking Water Applications, *Corros. Sci.*, 2014, **87**, p 6–10
15. I.G. Ogunsanya and C.M. Hansson, The Semiconductor Properties of Passive Films and Corrosion Behavior of Stainless Steel Reinforcing Bars in Simulated Concrete Pore Solution, *Materialia*, 2019, **6**, p 100321-1–100321-14
16. G. Tranchida, M. Clesi, F. Di Franco, F. Di Quarto, and M. Santamaria, Electronic Properties and Corrosion Resistance of Passive Films on Austenitic and Duplex Stainless Steels, *Electrochim. Acta*, 2018, **273**, p 412–423
17. R.A. Antunes, M.C.L. Oliveira, and I. Costa, Study of the Correlation Betweeen Corrosion Resistance and Semiconducting Properties of the Passive Film of AISI, 316L in Physiological Solution, *Mater. Corros.*, 2012, **63**, p 586–592
18. J. Zhang, X. Hu, and K. Chou, Effect of Thiosulfate on Corrosion Behavior and Passive Films of Duplex Stainless Steel 2205 in Chloride Solutions, *Int. J. Electrochem. Sci.*, 2019, **14**, p 9960–9973
19. N.B. Hakiki, S. Boudin, B. Rondot, and M. Da Cunha Belo, The Electronic Structure of Passive Films Formed on Stainless Steels, *Corros. Sci.*, 1995, **37**, p 1809–1822
20. H.-Y. Ha, J.H. Jang, T.-H. Lee, C. Won, C.-H. Lee, J. Moon, and C.-G. Lee, Investigation of the Localized Corrosion and Passive Behavior of Type 304 Stainless Steels with 0.2–1.8 wt% B, *Materials*, 2018, **11**, p 2097-1–2097-15
21. Y. Zhang, H. Luo, Q. Zhang, H. Yu, and J. Lv, Characterization of Passive Films Formed on As-Received and Sensitized AISI, 304 Stainless Steel, *Chin. J. Mech. Eng.*, 2019, **32**, p 27-1–27-12
22. R.M. Fernández-Domene, R. Sánchez-Tovar, C. Escrivà-Cerdán, R. Leiva-García, and J. García-Antón, Study of Passive Films Formed on AISI, 316L Stainless Steel in Non-polluted and Underwater-Volcano-Polluted Seawater, *Corrosion*, 2014, **70**, p 390–401
23. H. Xu, L. Wang, D. Sun, and H. Yu, The Passive Oxide Films Growth on 316L Steel in Borate Buffer Solution Measured by Real-Time Spectroscopic Ellipsometry, *Appl. Surf. Sci.*, 2015, **351**, p 367–373
24. A. Kocijan, C. Donik, and M. Jenko, Electrochemical and XPS Studies of the Passive Film Formed on Stainless Steels in Borate Buffer and Chloride Solutions, *Corros. Sci.*, 2007, **49**, p 2083–2098
25. C. Zhang, Z.-W. Zhang, and L. Liu, Degradation in Pitting Resistance of 316L Stainless Steel Under Hydrostatic Pressure, *Electrochim. Acta*, 2016, **210**, p 401–406
26. T. Hanawa, S. Hiromoto, A. Yamamoto, D. Kuroda, and K. Asami, XPS Characterization of the Surface Oxide Film of 316L Stainless Steel Samples that were Located in Quasi-Biological Environments, *Mater. Trans.*, 2002, **43**, p 3088–3092
27. W. Miao, Z. Gao, and W. Hu, Passivity and Pitting Corrosion of 316L in Simulated Concrete Pore Solutions Under Marine Environment, *Int. J. Electrochem. Sci.*, 2018, **13**, p 771–784
28. S. He and D. Jiang, Electrochemical Behavior and Properties of Passive Films on 304 Stainless Steel Under High Temperature and Stress Conditions, *Int. J. Electrochem. Sci.*, 2018, **13**, p 5832–5849
29. H. Luo, H. Su, C. Dong, K. Xiao, and X. Li, Electrochemical and Passivation Behavior Investigation of Ferritic Stainless Steel in Alcaline Environment, *Constr. Build. Mater.*, 2015, **96**, p 502–507
30. S.K. Bonagani, V. Kain, V. Bathula, R.H. Banerlee, and S. Tenneti, Electrochemical Behavior and Passive Property of 13Cr Martensitic Stainless Steel in Nitric Acid Solution, *J. Mater. Eng. Perform.*, 2020, **29**, p 215–229
31. P. Mills and J.L. Sullivan, A Study of the Core Level Electrons in Iron and Its Three Oxides by Means of X-Ray Photoelectron Spectroscopy, *J. Phys. D Appl. Phys.*, 1983, **16**, p 723–732
32. S. Habibzadeh, L. Li, D. Shum-Tim, E.C. Davis, and S. Omanovic, Electrochemical Polishing as a 316L Stainless Steel Surface Treatment Method: Towards the Improvement of Biocompatibility, *Corros. Sci.*, 2014, **87**, p 89–100
33. X. Feng, X. Lu, Y. Zuo, and D. Chen, The Passive Behaviour of 304 Stainless Steels in Saturated Calcium Hydroxide Solution Under Different Deformation, *Corros. Sci.*, 2014, **82**, p 347–355
34. X. Cheng, Z. Feng, C. Li, C. Dong, and X. Li, Investigation of Oxide Film Formation on 316L Stainless Steel in High-Temperature Aqueous Environments, *Electrochim. Acta*, 2011, **56**, p 5860–5865
35. A. Lasczynska, W. Tylus, J. Winiarski, and I. Szczygiel, Evolution of Corrosion Resistance and Passive Film Properties of Ni-Mo Alloy Coatings During Exposure to 0.5 M NaCl Solution, *Surf. Coat. Technol.*, 2017, **317**, p 26–37
36. X. Ren, K. Sridharan, and T.R. Allen, Corrosion of Ferritic-Martensitic Steel HT9 in Supercritical Water, *J. Nuclear Mater.*, 2006, **358**, p 227–234
37. B. Krawczyk, P. Cook, J. Hobbs, and D.L. Engelberg, Corrosion Behavior of Aqua-Blasted and Laser-Engraved Type 316L Stainless Steel, *J. Mater. Eng. Perform.*, 2017, **26**, p 6167–6181
38. S. Tardio, M.-L. Abel, R.H. Carr, J.E. Castle, and J.F. Watts, Comparative Study of the Native Oxide on 316L Stainless Steel by XPS and ToF-SIMS, *J. Vacuum Sci. Technol.*, 2015, **33**, p 05E122-1–05E122-14
39. J. Xu, C.G. Zhou, and S.Y. Jiang, Investigation on Corrosion Behavior of Sputter Deposited Nanocrystalline $(Mo_xCr_{1-x})_5Si_3$ Films by Double Cathode Glow Plasma, *Intermetallics*, 2010, **18**, p 1669–1675
40. X. Liu, X. Wu, and E.H. Han, Effect of Zn Injection on Established Surface Oxide Films on 316L Stainless Steel in Borated and Lithiated High Temperature Water, *Corros. Sci.*, 2012, **65**, p 136–144
41. Z. Duan, F. Arjmand, L. Zhang, and H. Abe, Investigation of the Corrosion Behavior of 304L and 316L Stainless Steels at High-Temperature Borated and Lithiated Water, *J. Nuclear Sci. Technol.*, 2015, **53**, p 1435–1446
42. H. Luo, H. Su, C. Dong, and K. Xiao, Electrochemical and Passivation Behavior Investigation of Ferritic Stainless Steel in Simulated Concrete Pore Media, *Data Brief*, 2015, **5**, p 171–178
43. R.I. Revilla, B. Wouters, F. Andreatta, A. Lanzutti, L. Fedrizzi, and I. de Graeve, EIS Comparative Study and Critical Equivalent Electrical Circuit (EEC) Analysis of the Native Oxide Layer of Additive Manufactured and Wrought 316L Stainless Steel, *Corros. Sci.*, 2020, **167**, p 108480
44. S. Wang, Y. Hu, K. Fang, W. Zhang, and X. Wang, Effect of Surface Machining on the Corrosion Behaviour of 316 Austenitic Stainless Steel in Simulated PWR Water, *Corros. Sci.*, 2017, **126**, p 104–120
45. C.O.A. Olsson and D. Landolt, Passive Films on Stainless Steels—Chemistry, Structure and Growth, *Electrochim. Acta*, 2003, **48**, p 1093–1104
46. H. Luo, X. Wang, C. Dong, K. Xiao, and X. Li, Effect of Cold Deformation on the Corrosion Behavior of UNS S31803 Duplex Stainless Steel in Simulated Concrete Pore Solution, *Corros. Sci.*, 2017, **124**, p 178–192
47. L.V. Taveira, M.F. Montemor, D. da Cunha Belo, M.G. Ferreira, and L.F.P. Dick, Influence of Incorporated Mo and Nb on the Mott-Schottky Behaviour of Anodic Films Formed on AISI, 304L, *Corros. Sci.*, 2010, **52**, p 2813–2818
48. D.D. Macdonald, Passivity—The Key to Our Metals-Based Civilization, *Pure Appl. Chem.*, 1999, **71**, p 951–978
49. L. Liu, J. Xu, X. Lu, P.R. Munroe, and Z. Xie, Electrochemical Corrosion Behavior of Nanocrystalline β-Ta Coating for Biomedical Applications, *ACS Biomater. Sci. Eng.*, 2016, **2**, p 579–594
50. K. Shi, Y. Zhang, J. Zhang, and Z. Xie, Electrochemical Properties of Niobium Coating for Biomedical Application, *Coatings*, 2019, **9**, p 546-1–546-15
51. M.J. Carmezim, A.M. Simões, M.F. Montemor, and M. Da Cunha Belo, Capacitance Behavior of Passive Films on Ferritic and Austenitic Stainless Steel, *Corros. Sci.*, 2005, **47**, p 581–591
52. W. Ye, Y. Li, and F. Wang, The Improvement of the Corrosion Resistance of 309 Stainless Steel in the Transpassive Region by Nano-Crystallization, *Electrochim. Acta*, 2009, **54**, p 1339–1349
53. Z. Ai, W. Sun, J. Jiang, D. Song, H. Ma, J. Zhang, and D. Wang, Passivation Characteristics of Alloy Corrosion-Resistant Steel Cr10Mo1 in Simulating Concrete Pore Solutions: Combination Effects of pH and Chloride, *Materials*, 2016, **9**, p 749-1–749-17
54. D.G. Li, J.D. Wang, D.R. Chen, and P. Liang, Molybdenum Addition Enhancing the Corrosion Behaviors of 316 L Stainless Steel in the

Simulated Cathodic Environment of Proton Exchange Membrane Fuel Cell, *Int. J. Hydrogen Energy*, 2015, **40**, p 5947–5957
55. J. Lv, Z. Wang, T. Liang, K. Suzuki, and H. Miura, Enhancing the Corrosion Resistance of the 2205 Duplex Stainless Steel Bipolar Plates in PEMFCs Environment by Surface Enriched Molybdenum, *Results Phys.*, 2017, **7**, p 3459–3464
56. V. Vignal, J.M. Olive, and D. Desjardins, Effect of Molybdenum on Passivity of Stainless Steels in Chloride Media Using Ex Situ Near Field Microscopy Observations, *Corros. Sci.*, 1999, **41**, p 869–884
57. A. Kocijan, C. Donik, and M. Jenko, The Corrosion Behaviour of Duplex Stainless Steel in Chloride Solutions Studied by XPS, *Mater. Technol.*, 2009, **43**, p 195–199
58. E. De Vito and P. Marcus, XPS Study of Passive Films Formed on Molybdenum-Implanted Austenitic Stainless Steels, *Surf. Int. Anal.*, 1992, **19**, p 403–408
59. A. Bautista, G. Blanco, F. Velasco, A. Gutiérrez, L. Soriano, F.J. Palomares, and H. Takenout, Changes in the Passive Layer of Corrugated Austenitic Stainless Steel of Low Nickel Content Due to Exposure to Simulated Pore Solutions, *Corros. Sci.*, 2009, **51**, p 785–792
60. M. Liu, X. Cheng, X. Li, Y. Pan, and J. Li, Effect of Cr on the Passive Film Formation Mechanism of Steel Rebar in Saturated Calcium Hydroxide Solution, *Appl. Surf. Sci.*, 2016, **389**, p 1182–1191
61. M. Liu, S. Luo, H. Zhang, and H. Chen, Effect of CO_2 and H_2S on the Corrosion Resistance of FV520B Steel in Salinity Water, *Int. J. Electrochem. Sci.*, 2019, **14**, p 4838–4851
62. J. Lv and H. Luo, Comparison of Corrosion Properties of Passive Films Formed on Phase Reversion Induced Nano/Ultrafine-Grained 321 Stainless Steel, *Appl. Surf. Sci.*, 2013, **280**, p 123–131
63. S. Ningshen, U.K. Mudali, V.K. Mittal, and H.S. Khatak, Semiconducting and Passive Film Properties of Nitrogen-Containing Type 316LN Stainless Steels, *Corros. Sci.*, 2007, **49**, p 481–496
64. H.X. Guo, B.T. Lu, and J.L. Luo, Study on Passivation and Erosion-Enhanced Corrosion Resistance by Mott-Schottky Analysis, *Electrochim. Acta*, 2006, **52**, p 1108–1116
65. Z. Feng, X. Cheng, C. Dong, L. Xu, and X. Li, Passivity of 316L Stainless Steel in Borate Buffer Solution Studied by Mott-Schottky Analysis, Atomic Absorption Spectrometry and X-Ray Photoelectron Spectroscopy, *Corros. Sci.*, 2010, **52**, p 3646–3653
66. M.J. Carmezim, A.M. Simões, M.O. Figueiredo, and M. Da Cunha Belo, Electrochemical Behaviour of Thermally Treated Cr-Oxide Films Deposited on Stainless Steel, *Corros. Sci.*, 2002, **44**, p 451–465

Publisher's Note Springer Nature remains neutral with regard to jurisdictional claims in published maps and institutional affiliations.